

# Wetting and capillary nematization of binary hard-platelet and hard-rod fluids

L. Harnau\* and S. Dietrich

*Max-Planck-Institut für Metallforschung, Heisenbergstrasse 1, D-70569 Stuttgart, Germany,  
and Institut für Theoretische und Angewandte Physik, Universität Stuttgart,  
Pfaffenwaldring 57, D-70569 Stuttgart, Germany*

(Dated: October 26, 2018)

Density-functional theory is used to investigate the phase behavior of colloidal binary hard-platelet and hard-rod fluids near a single hard wall or confined in a slit pore. The Zwanzig model, in which the orientations of the particles of rectangular shape are restricted to three orthogonal orientations, is analyzed by numerical minimization of the grand potential functional. The density and orientational profiles as well as the surface contributions to the grand potential are determined. The calculations exhibit a wall-induced continuous surface transition from uniaxial to biaxial symmetry for the hard-rod fluid. Complete wetting of the wall – isotropic liquid interface by a biaxial nematic film for rods and a uniaxial nematic film for platelets is found. For the fluids confined by two parallel hard walls we determine a first-order capillary nematization transition for large slit widths, which terminates in a capillary critical point upon decreasing the slit width.

PACS numbers: 61.20.-p, 61.30.Gd, 82.70.Dd

## I. INTRODUCTION

Many complex fluids used in industry or in soft condensed-matter laboratories consist of non-spherical colloidal particles [1]. In particular suspensions of hard platelike colloidal particles have recently received experimental [2, 3, 4, 5, 6] and theoretical attention [7, 8, 9, 10, 11, 12], because of the rich phase behavior and the geophysical and technological implications. It has been shown experimentally [5], theoretically [10], and by simulation [7], that polydispersity in the size of the platelets strongly affects the phase behavior. Whereas the theoretical studies have focused on the understanding of the interactions and the phase behavior of homogeneous bulk fluids, experimentally it turns out that boundaries such as the walls of the sample cells have a pronounced influence on the phase behavior [2, 4, 5]. Liquid-liquid or wall-liquid interfaces are intrinsic inhomogeneities of the experimental samples which have been studied recently [2, 3, 4, 5, 6].

Here we study inhomogeneous colloidal fluids consisting of non-spherical particles by examining both binary hard-platelet and binary hard-rod fluids within the Zwanzig model [13]. Platelets or rods are represented by square parallelepipeds and the allowed orientations of the normal of the particles along their main axis of symmetry are restricted to three mutually perpendicular directions, rather than a continuous range of orientations in space (see Fig. 1). Zwanzig's model may be considered as a coarse-grained version of the Onsager model which allows for continuously varying orientations [14]. Zwanzig's model offers the advantage that the difficult determination of inhomogeneous density profiles becomes numerically straightforward, allowing one to study various as-

pects of inhomogeneous binary hard-platelet and binary hard-rod fluids in detail. On the basis of recent experience with monodisperse hard-rod fluids [15, 16, 17] the Zwanzig model is expected to provide a qualitatively correct description of the aforementioned colloidal suspensions by focusing on the entropic properties. In studying both binary platelet fluids and binary rod fluids we address the problem of a possible surface transition from uniaxial to biaxial symmetry. To the best of our knowledge properties of binary rod fluids near a hard wall or in a slit pore have also not been studied before. Our study provides a direct comparison of the structural properties and of the behavior of fluids consisting of rodlike and platelike particles, respectively.

In Sec. II we describe the density-functional theory and the third-order virial excess free energy functional. Section III presents bulk phase diagrams of binary mixtures of thin platelets and binary mixtures of thin rods, showing how the density gap at the isotropic-nematic transition varies with the mole fraction of the larger particles. In Sec. IV we determine the density and orientational profiles as well as the excess adsorptions of the fluids near a hard wall. The calculations exhibit a wall-induced surface transition from uniaxial to biaxial symmetry for fluids consisting of rods. Binary hard-rod and binary hard-platelet fluids confined by two parallel hard walls are investigated in Sec. V. For sufficiently large slit widths a first-order capillary nematization transition is found. Our results are summarized in Sec. VI.

## II. DENSITY FUNCTIONAL FOR THE ZWANZIG MODEL

We consider a binary mixture of hard rectangular particles of size  $L_i \times D_i \times D_i$  ( $i = 1, 2$ ) [13]. The number density of the centers of mass of the particles of species  $i$  at a point  $\mathbf{r}$  is denoted by  $\rho_\beta^{(i)}(\mathbf{r})$ . The number den-

---

\*Electronic address: harnau@fluids.mpi-stuttgart.mpg.de

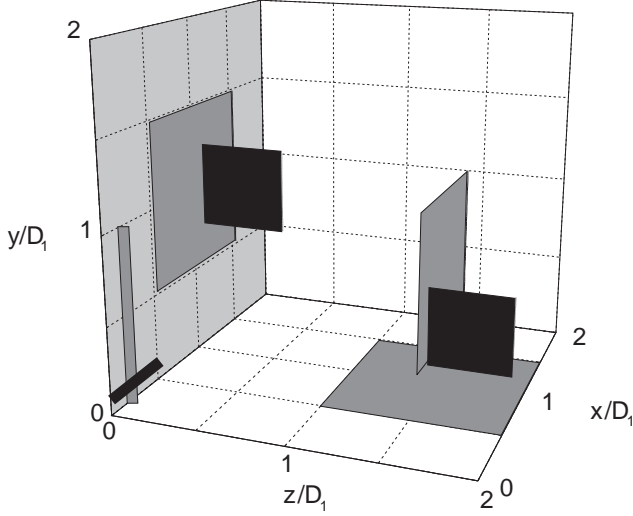


FIG. 1: The system under consideration consists of a binary fluid of thin platelets of surface sizes  $D_1 \times D_1$  (gray squares) and  $D_2 \times D_2$  (black squares) in contact with a planar hard wall at  $z = 0$ . The figure displays configurations contributing to the second order virial term  $\rho_x^{(2)}(z_1)\rho_z^{(1)}(z_2)$  [left], and the third order virial term  $\rho_x^{(2)}(z_1)\rho_y^{(1)}(z_2)\rho_z^{(1)}(z_3)$  [right] for  $D_1 = 2D_2$ . For comparison a configuration contributing to the second order virial term  $\rho_x^{(2)}(z_1)\rho_y^{(1)}(z_2)$  of a binary rod fluid is shown. Within this model of only three discrete orientations particles lying very close to the wall must adopt a fully parallel alignment.

sity of the centers of mass of the particles of species  $i$  at a point  $\mathbf{r}$  is denoted by  $\rho_\beta^{(i)}(\mathbf{r})$ . The position of the center of mass  $\mathbf{r}$  is continuous, while the allowed orientations of the normal of the particles along their main axis of symmetry is restricted to directions  $\beta = x, y, z$ . The equilibrium density profiles of the mixture under the influence of external potentials  $V_\beta^{(i)}(\mathbf{r})$  minimize the grand potential functional

$$\Omega[\rho_\beta^{(i)}(\mathbf{r})] = \sum_{i=1}^2 \sum_{\beta} \int d\mathbf{r} \rho_\beta^{(i)}(\mathbf{r}) \left[ k_B T \left( \ln[\Lambda_i^3 \rho_\beta^{(i)}(\mathbf{r})] - 1 \right) - \mu_i + V_\beta^{(i)}(\mathbf{r}) \right] + F_{ex}[\rho_\beta^{(i)}(\mathbf{r})], \quad (1)$$

where  $\Lambda_i$  are the thermal de Broglie wavelengths and  $\mu_i$  are the chemical potentials. Within a third order virial approximation the excess free energy functional

$F_{ex}[\rho_\beta^{(i)}(\mathbf{r})]$  is given by

$$F_{ex}[\rho_\beta^{(i)}(\mathbf{r})] = -\frac{k_B T}{2} \sum_{i,j=1}^2 \sum_{\beta_1, \beta_2} \int d\mathbf{r}_1 d\mathbf{r}_2 f_{\beta_1, \beta_2}^{(i,j)}(\mathbf{r}_1, \mathbf{r}_2) \rho_{\beta_1}^{(i)}(\mathbf{r}_1) \rho_{\beta_2}^{(j)}(\mathbf{r}_2) \times \left[ 1 + \frac{1}{3} \sum_{k=1}^2 \sum_{\beta_3} \int d\mathbf{r}_3 f_{\beta_2, \beta_3}^{(j,k)}(\mathbf{r}_2, \mathbf{r}_3) f_{\beta_3, \beta_1}^{(k,i)}(\mathbf{r}_3, \mathbf{r}_1) \rho_{\beta_3}^{(k)}(\mathbf{r}_3) \right], \quad (2)$$

where  $f_{\beta_1, \beta_2}^{(i,j)}(\mathbf{r}_1, \mathbf{r}_2)$  is the Mayer function. The Mayer function equals  $-1$  if the particles overlap and is zero otherwise. With the definition  $S_{\alpha, \beta}^{(i)} = D_i + (L_i - D_i)\delta_{\alpha, \beta}$ , which represents the spatial extent in direction  $\alpha = x, y, z$  of a particle with orientation  $\beta$  of the normal, the Mayer function can be written explicitly as

$$f_{\beta_1, \beta_2}^{(i,j)}(\mathbf{r}_1, \mathbf{r}_2) = -\prod_{\alpha=1}^3 \Theta \left( \frac{1}{2} \left( S_{\alpha, \beta_1}^{(i)} + S_{\alpha, \beta_2}^{(j)} \right) - |r_{\alpha,1} - r_{\alpha,2}| \right), \quad (3)$$

where  $r_{\alpha,1}$  is the projection of the position vector  $\mathbf{r}_1$  in  $\alpha$  direction and  $\Theta(r)$  is the Heaviside step function. The density functional theory is completely specified by the excess free energy functional and the Mayer function. The necessity for including the third order density term in Eq. (2), which is not present in the Onsager second virial approximation [14] used in the description of thin rods, already follows from recent calculations of equilibrium properties of a homogeneous fluid consisting of monodisperse thin platelets [9].

For model systems of hard particles near a structureless wall at  $z = 0$ , apart from a possible surface freezing at high densities, nonuniformities of the density occur only in the  $z$  direction, so that  $\rho_\beta^{(i)}(\mathbf{r}) = \rho_\beta^{(i)}(z)$ . Hence the excess free energy functional can be written as

$$F_{ex}[\rho_\beta^{(i)}(z)] = -\frac{k_B T}{2} \sum_{i,j=1}^2 \sum_{\beta_1, \beta_2} \int dz_1 dz_2 l_{\beta_1, \beta_2}^{(i,j)}(z_1, z_2) \rho_{\beta_1}^{(i)}(z_1) \rho_{\beta_2}^{(j)}(z_2) \times \left[ 1 + \frac{1}{3A} \sum_{k=1}^2 \sum_{\beta_3} \int dz_3 l_{\beta_2, \beta_3}^{(j,k)}(z_2, z_3) l_{\beta_3, \beta_1}^{(k,i)}(z_3, z_1) \rho_{\beta_3}^{(k)}(z_3) \right] \quad (4)$$

with

$$l_{\beta_1, \beta_2}^{(i,j)}(z_1, z_2) = \int dx_1 dy_1 dx_2 dy_2 f_{\beta_1, \beta_2}^{(i,j)}(\mathbf{r}_1, \mathbf{r}_2) = -A \left( S_{x, \beta_1}^{(i)} + S_{x, \beta_2}^{(j)} \right) \left( S_{y, \beta_1}^{(i)} + S_{y, \beta_2}^{(j)} \right) \times \Theta \left( \frac{1}{2} \left( S_{z, \beta_1}^{(i)} + S_{z, \beta_2}^{(j)} \right) - |z_1 - z_2| \right), \quad (5)$$

where  $A$  is the macroscopic surface area in the  $x - y$  plane. The particular factorization of the Mayer function (3), which results from both particle shape and restricted orientations, leads to the relative simplicity of the functions  $l_{\beta_1, \beta_2}^{(i, j)}(z_1, z_2)$ . Figure 1 displays a second and third order virial contribution schematically.

Third order virial contributions for thin rods ( $D_i \ll L_j$ ,  $i, j = 1, 2$ ) are negligible due to the small intermolecular interaction between rods [13, 14]. For thin platelets ( $L_i \ll D_j$ ,  $i, j = 1, 2$ ) the truncation of the virial expansion after the second order cannot be justified because of the nonzero probability of intersection even at small thickness  $L_i$  (see Fig. 1).

### III. ISOTROPIC AND NEMATIC BULK PHASES

Based on the density functional in Eqs. (1), (4), and (5) we study first the homogeneous bulk fluid with  $V_\beta^{(i)}(\mathbf{r}) = 0$  in a macroscopic volume  $V$ . The equilibrium profiles are then constant ( $\rho_\beta^{(i)}(\mathbf{r}) = \rho_\beta^{(i)}$ ) and the Euler-Lagrange equations resulting from the stationarity conditions  $\partial\Omega[\rho_\beta^{(i)}]/\partial\rho_\beta^{(i)} = 0$  for the binary platelet mixture read ( $\beta_1 \neq \beta_2 \neq \beta_3$ ,  $i \neq j$ ):

$$\begin{aligned} \ln(\Lambda_i^3 \rho_{\beta_1}^{(i)}) = & \\ & \mu_i (k_B T)^{-1} - 2D_i^3 \left[ \rho_{\beta_2}^{(i)} + \rho_{\beta_3}^{(i)} \right] \\ & - D_i D_j (D_i + D_j) \left[ \rho_{\beta_2}^{(j)} + \rho_{\beta_3}^{(j)} \right] - D_i^6 \rho_{\beta_2}^{(i)} \rho_{\beta_3}^{(i)} \\ & - D_i^2 D_j^4 \rho_{\beta_2}^{(j)} \rho_{\beta_3}^{(j)} - D_i^4 D_j^2 \left[ \rho_{\beta_2}^{(i)} \rho_{\beta_3}^{(j)} + \rho_{\beta_2}^{(j)} \rho_{\beta_3}^{(i)} \right]. \end{aligned} \quad (6)$$

The Euler-Lagrange equations for a binary mixture of thin rectangular rods ( $D = D_i = D_j$ ) are given by [18]:

$$\begin{aligned} \ln(\Lambda_i^3 \rho_{\beta_1}^{(i)}) = & \mu_i (k_B T)^{-1} - 2L_i^2 D \left[ \rho_{\beta_2}^{(i)} + \rho_{\beta_3}^{(i)} \right] \\ & - 2L_i L_j D \left[ \rho_{\beta_2}^{(j)} + \rho_{\beta_3}^{(j)} \right]. \end{aligned} \quad (7)$$

The Euler-Lagrange equations (6) for the platelet mixture are independent of the platelet thickness  $L_i$  because the integrals over Mayer functions in Eq. (2) are independent of  $L_i$  for thin platelets. For example, the integral over the Mayer function of two particles of species  $i$  orthogonal to each other is given by

$$V_{x,z}^{(i,i)} = \int d\mathbf{r}_1 f_{x,z}^{(i,i)}(\mathbf{r}_1, 0) = 2D_i(L_i + D_i)^2. \quad (8)$$

In the limit of thin platelets ( $L_i \ll D_i$ ) the integral over the Mayer function reduces to  $V_{x,z}^{(i,i)} \approx 2D_i^3$ , which is the prefactor of the second term on the right side of Eq. (6). In other words, thin platelets have an excluded volume (the volume which is denied to a platelet by the condition that it must not intersect another platelet), although they have a vanishing volume  $L_i D_i^2$  (see Fig. 1). On the

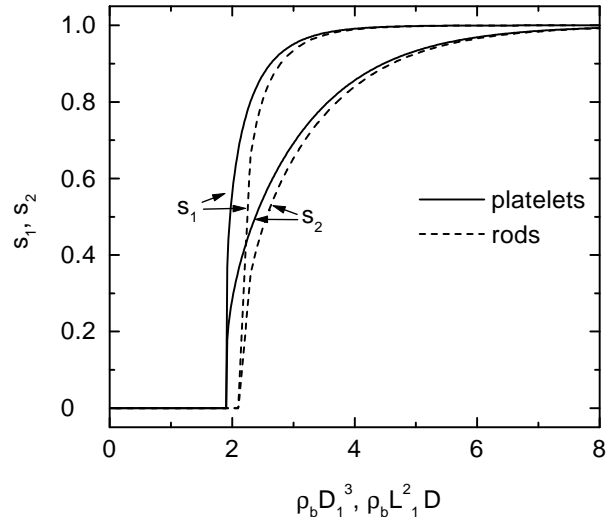


FIG. 2: Relative bulk nematic order parameters  $s_1$  (upper curves) and  $s_2$  (lower curves) for a binary mixture of thin rectangular platelets (solid curves,  $D_1 = 2^{2/3} D_2$ ) and thin rectangular rods (dashed curves,  $L_1 = 2L_2$ ,  $L_1/D \rightarrow \infty$ ). The number densities of the larger and the smaller particles are fixed to  $\rho_1 = \rho_2$ . Isotropic orientations at low densities are characterized by  $s_i = 0$ , while nematic ordering ( $0 < s_i \leq 1$ ) is preferred for higher densities.

other hand, the integrals over Mayer functions and the excluded volume of thin rods depend on both  $L_i$  and  $D_i$ :  $V_{x,z}^{(i,i)} \approx 2L_i^2 D_i$ . We have solved Eqs. (6) and (7) numerically for given chemical potentials. For convenience the total number density  $\rho_b = \sum_i \sum_\beta \rho_\beta^{(i)}$  and the number densities  $\rho_i$  of particles of species  $i$  are introduced according to:  $\rho_i = \rho_x^{(i)} + \rho_y^{(i)} + \rho_z^{(i)}$ ,  $\rho_1 + \rho_2 = \rho_b$ . The theory has been formulated in a way that is completely symmetrical with respect to the three coordinate axis. Hence there must be a corresponding threefold degeneracy in the results. We define the  $z$  axis as the preferred coordinate axis and consider the relative uniaxial nematic order parameters  $s_i = [\rho_z^{(i)} - (\rho_x^{(i)} + \rho_y^{(i)})/2]/\rho_i$ . A typical set of  $(s_1, s_2)$  as a function of  $\rho_b$ , with  $\rho_1 = \rho_2$ ,  $L_1 = 2L_2$  for rods and  $D_1 = 2^{2/3} D_2$  for platelets is shown in Fig. 2. The size ratios of the rods and platelets have been fixed such that the second virial coefficients  $b_2$  of the equation of state of the monodisperse fluids ( $\rho_2 = 0$ ) in the isotropic phase are equal:

$$\Omega = -\rho_b [1 + b_2 \rho_b + b_3 \rho_b^2] k_B T V, \quad (9)$$

with  $b_2 = 2L_1^2 D/3$  for thin rods, and  $b_2 = 2D_1^3/3$  for thin platelets. For small values of  $\rho_b$  the isotropic phase ( $s_1 = s_2 = 0$ ) is stable. At a critical density another set of solutions, with  $0 < s_i \leq 1$ , appears which represents the more favorable nematic phases. The isotropic-nematic (IN) transition of the binary platelet mixture takes place at a smaller density than for the rod mixture. We notice that the chemical potentials  $\mu_i$  can be

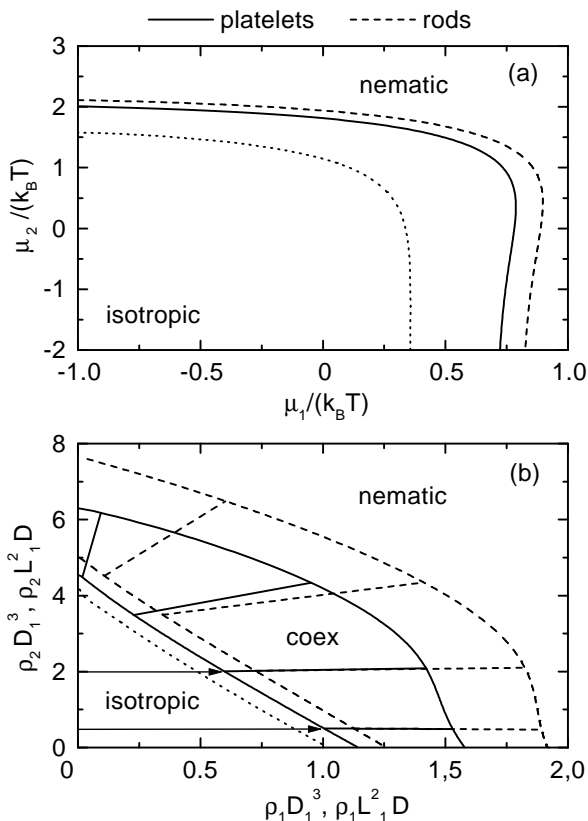


FIG. 3: (a) Bulk phase diagram of a fluid consisting of a binary mixture of thin platelets (solid curve,  $D_1 = 2^{2/3}D_2$ ) and a binary mixture of thin rods (dashed curve,  $L_1 = 2L_2$ ,  $L_1/D \rightarrow \infty$ ) as a function of the chemical potentials  $\mu_1$  and  $\mu_2$ . (b) Bulk phase diagram of the same fluids in the density-density, i.e.,  $\rho_1 - \rho_2$  plane (with the same line code as in (a)). The straight lines are tielines illustrating isotropic-nematic coexistence. In (a) and (b) the dotted lines mark the locations of the uniaxial-biaxial transition densities of the binary rod fluid in contact with a hard wall. In Figs. 5 and 6 excess adsorptions near a hard wall are shown along the two thermodynamic paths indicated by arrows.

written as a function of  $s_i$  and  $\rho_i$  using Eqs. (6) and (7). At this point it is convenient to introduce the variables  $\mu_i^* = \mu_i - k_B T \ln(\Lambda_i^3/c_i)$ , where  $c_i = L_1^2 D$  for the rod fluid and  $c_i = D_1^3$  for the platelet fluid. In the following numerical data are given in terms of  $\mu_i^*$  and we drop the star in order to avoid a clumsy notation. The compositions, densities, order parameters, and thermodynamic properties of the IN coexistence phases are found by solving the coexistence conditions:  $\mu_{iI} = \mu_{iN}$  and  $p_I = p_N$  where  $\mu_{iI}$ ,  $\mu_{iN}$  and  $p_I = -\Omega_I/V$ ,  $p_N = -\Omega_N/V$  are the chemical potentials and the pressure of the isotropic and the nematic phase, respectively. The phase diagrams for binary platelet and binary rod mixtures are displayed in Fig. 3. The calculations render the concentration in the isotropic phase always to be less than in the nematic phase. For monodisperse platelet fluids the density gap at the IN transition  $\Delta\rho = (\rho^{(N)} - \rho^{(I)})/\rho^{(I)} = 0.23$  is smaller

than the one for monodisperse rod fluids ( $\Delta\rho = 0.52$ ). The different size of the density gap is due to larger intermolecular interactions between platelets as compared with those between rods. Moreover, a widening of the IN coexistence region is observed at intermediate values of the mole fraction of the larger particles. With increasing the size ratios of the particles ( $L_1 = 3L_2$ ,  $D_1 = 3^{2/3}D_2$ ) the calculations exhibit a greater degree of fractionation between the two coexisting phases. The smaller particles are preferentially in the isotropic phase. The results for rods are in agreement with earlier calculations [18].

#### IV. HARD-ROD AND HARD-PLATELET FLUIDS NEAR A HARD WALL

The density and orientational profiles of both components of binary hard-rod and binary hard-platelet mixtures close to a planar hard wall are obtained by a numerical minimization of the grand potential functional (1) with the excess free energy functional (4). The results are conveniently expressed in terms of the orientationally averaged number density profiles

$$\rho_i(z) = \rho_x^{(i)}(z) + \rho_y^{(i)}(z) + \rho_z^{(i)}(z), \quad (10)$$

position-dependent nematic order parameters

$$s_i(z) = \frac{\rho_z^{(i)}(z) - 0.5[\rho_x^{(i)}(z) + \rho_y^{(i)}(z)]}{\rho_i(z)}, \quad (11)$$

and position-dependent biaxial order parameters

$$q_i(z) = \frac{\rho_x^{(i)}(z) - \rho_y^{(i)}(z)}{\rho_i(z)}. \quad (12)$$

At small distances from the wall the value of the nematic order parameter reflects the geometric constraints. A platelet [rod] lying very closely to the wall must adopt a fully parallel alignment (see Fig. 1), so that the nematic order parameters reach their limiting values  $s_i(0) = 1$  [ $s_i(0) = -1/2$ ] there, whereas the isotropic orientation  $s_i(z) = 0$  is attained at large distances from the wall. Orientational profiles of biaxial symmetry are described by  $s_i(z) \neq 0$ ,  $q_i(z) \neq 0$ , where a positive or negative sign of  $q_i(z)$  signals a spontaneous preferential alignment of the normals parallel to the  $x$ -axis or  $y$ -axis, respectively.

##### A. Monodisperse fluids

The phase behavior of monodisperse hard-rod fluids ( $\rho_2(z) = 0$ ) near a structureless wall has been investigated using the Zwanzig model and a wall-induced transition from uniaxial to biaxial symmetry upon increasing the bulk density has been found [15, 16]. Moreover, we have recently investigated both monodisperse hard-platelet fluids and monodisperse hard-rod fluids near a structureless wall at low bulk densities using a model that

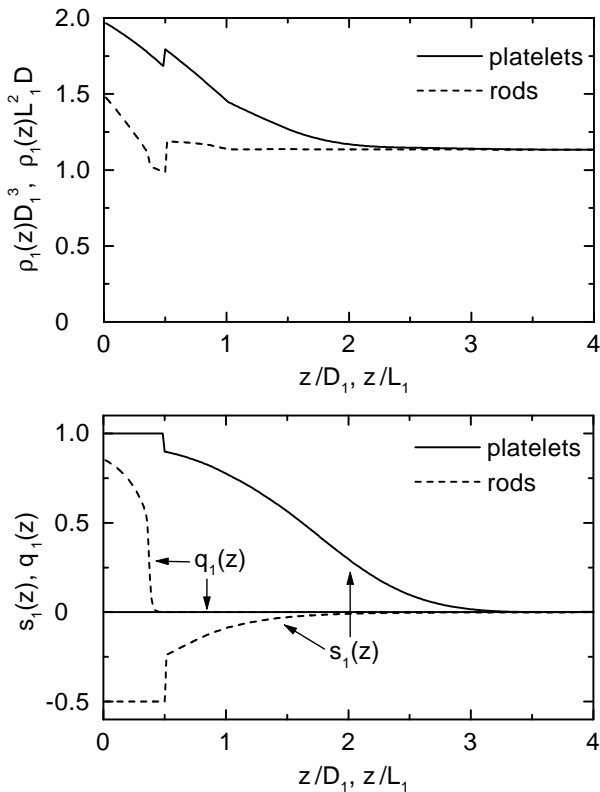


FIG. 4: Orientationally averaged number density profiles  $\rho_1(z)$ , nematic order parameters  $s_1(z)$ , and biaxial order parameters  $q_1(z)$  for monodisperse thin platelets (solid curves) and thin rods (dashed curves,  $D/L_1 \rightarrow \infty$ ) in contact with a planar hard wall at  $z = 0$ . Positive [negative] values of the nematic order parameters indicate that the platelets [rods] are preferentially aligned parallel to the wall. Biaxial symmetry of rods near the wall is characterized by  $q_1(z) \neq 0$ . Here  $q_1(z) \neq 0$  for  $z > L_1/2$ . The bulk density is fixed to  $\rho_1 D_1^3 = 1.13$  for the platelets and  $\rho_1 L_1^2 D = 1.13$  for the rods.

allows for continuous orientations of the particles [12]. Here we extend these previous calculations and present in Fig. 4 the calculated order parameters of monodisperse hard-platelet fluids and monodisperse hard-rod fluids for high bulk densities. The sharp cusps at  $z = D_1/2$  for platelets, and at  $z = L_1/2$  for rods, reflect the discontinuities of  $\rho_x^{(1)}(z)$  and  $\rho_y^{(1)}(z)$  for platelets, and of  $\rho_z^{(1)}(z)$  for rods, which determine the value of the nematic order parameters close to the wall. The most noteworthy feature is that no biaxiality is found for the platelet fluid ( $q_1(z) = 0$ ) while the loss of translational invariance due to the hard wall breaks the uniaxial symmetry of the rod fluid ( $q_1(z) \neq 0$ ). In order to study the possible onset of biaxiality, we rewrite the Euler-Lagrange equations in terms of the orientationally averaged number density

profile and of the order parameters:

$$\ln[\Lambda_1^3 \rho_x^{(1)}(z)] - \ln[\Lambda_1^3 \rho_y^{(1)}(z)] = \ln \left[ \frac{1 - s_1(z) + \frac{3}{2} q_1(z)}{1 - s_1(z) - \frac{3}{2} q_1(z)} \right] \equiv \Delta_1(z), \quad (13)$$

with

$$\Delta_1(z) = 2L_1^2 D \rho_1(z) q_1(z) \quad (14)$$

for the hard-rod fluid and

$$\Delta_1(z) = \frac{1}{D_1} \int_{z-D_1}^{z+D_1} dz_1 D_1^3 \rho_1(z_1) [q_1(z_1) + \frac{4}{D_1} \int_{z-\frac{D_1}{2}}^{z+\frac{D_1}{2}} dz_2 \Theta \left( \frac{D_1}{2} - |z_1 - z_2| \right) q_1(z_2)] \quad (15)$$

for the hard-platelet fluid. One easily finds that the uniaxial distribution, with  $q_1(z) = 0$ , is a solution of Eqs. (14) and (15) for any density  $\rho_1(z)$  and nematic order profile  $s_1(z)$ . Biaxial distributions  $q_1(z) \neq 0$  for the rod fluid are possible if  $\rho_1(z) \geq \rho_1^{(UB)}(z)$ , where the uniaxial-biaxial (UB) transition density  $\rho_1^{(UB)}(z)$  follows from a low- $q_1$  expansion of  $\Delta_1(z) = 3q_1(z)/[1 - s_1(z)] + O(q_1^3(z))$  for  $s_1(z) \neq 1$ :

$$\rho_1^{(UB)}(z) = \frac{3}{2[1 - s_1(z)]L_1^2 D}. \quad (16)$$

Since  $s_1(z) = -1/2$  ( $0 \leq z \leq L_1/2$ ) is the minimum value of  $s_1(z)$  for rods and because  $\rho_1^{(UB)}(z)$  decreases with decreasing  $s_1(z)$ , it follows that local biaxiality starts to develop if  $\rho_1(z) = 1$  in the interval  $0 \leq z \leq L_1/2$  (see Fig. 4). For platelets the value  $s_1(z) = 1$  ( $0 \leq z \leq D_1/2$ ) is determined by the geometric constraint. Hence  $q_1(z) = 0$  is the only solution of Eqs. (13) and (15) close to the wall.

## B. Binary fluids

The binary fluids considered in this subsection consist either of two types of thin rods ( $L_1 = 2L_2$ ) or of two types of thin platelets ( $D_1 = 2^{2/3}D_2$ ). We focus on the numerically determined excess adsorptions defined as

$$\Gamma_i = \int_0^\infty dz [\rho_i(z) - \rho_i], \quad (17)$$

where  $\rho_i = \rho_i(z \rightarrow \infty)$ . Figures 5 and 6 display  $\Gamma_i$  for binary rod fluids and binary platelet fluids, respectively. For a fixed bulk density of the small particles  $\rho_2$  and for small bulk densities of the large particles  $\rho_1$ , the excess adsorption of the small particles increases upon

increasing  $\rho_1$ . The reason for this is that the increasing number of large particles lying close to the wall enforces the orientational ordering of the small particles, leading to an enrichment of small particles near the wall because of reduced intermolecular interactions between the latter as compared to the isotropic bulk fluid. Due to the same mechanism,  $\Gamma_1$  increases upon increasing  $\rho_2$  for constant bulk densities of the large particles  $\rho_1$ . The excess adsorption of the large particles exhibits a change of sign and sharp increase with increasing  $\rho_1$  while a net depletion of the small particles is found for small bulk densities  $\rho_2$ . The calculation renders  $\Gamma_1$  to diverge logarithmically as  $\rho_1 \rightarrow \rho_1^{(I)}$ , where  $\rho_1^{(I)}$  is the bulk density of the large particles in the isotropic phase at the IN transition (see lower curves in the upper figure of Fig. 3). Near  $\rho_1^{(I)}$  the excess coverage can be fitted by  $\Gamma_1 = A_1 - A_2 \ln(L_1^2 D [\rho_1^{(I)} - \rho_1])$  for the rod fluid and  $\Gamma_1 = B_1 - B_2 \ln(D_1^3 [\rho_1^{(I)} - \rho_1])$  for the platelet fluid, with fit parameters  $A_1, A_2$  and  $B_1, B_2$ , while the excess coverage of the small particles remains finite and attains the critical value  $\Gamma_2^{(c)}$  via a square-root cusp singularity  $\Gamma_2 - \Gamma_2^{(c)} \sim \sqrt{\rho_1^{(I)} - \rho_1}$ . The logarithmic increase of  $\Gamma_1$  is consistent with complete wetting of the wall – isotropic fluid interface by a nematic film at  $\rho_1^{(I)}$ . Complete wetting is confirmed explicitly by the vanishing of the contact angle (see Sec. IV). One observes that the UB transition of the rods marks the onset of a pronounced variation of  $\Gamma_1$ , while  $\Gamma_1$  increases more smoothly upon increasing  $\rho_1$  for the binary platelet fluid, due to the absence of biaxiality. In order to study the possible onset of biaxiality for the binary rod fluid, we rewrite the Euler-Lagrange equations in terms of the density profiles and order parameters:

$$\begin{aligned} \ln \left[ \frac{1 - s_1(z) + \frac{3}{2}q_1(z)}{1 - s_1(z) - \frac{3}{2}q_1(z)} \right] &= \\ \frac{L_1}{L_2} \ln \left[ \frac{1 - s_2(z) + \frac{3}{2}q_2(z)}{1 - s_2(z) - \frac{3}{2}q_2(z)} \right] & \\ = 2D[L_1^2 \rho_1(z)q_1(z) + 2L_2^2 \rho_2(z)q_2(z)]. & \quad (18) \end{aligned}$$

For any  $s_i(z)$  and  $\rho_i(z)$  there is a trivial uniaxial solution  $q_i(z) = 0$  to Eq. (18). Nontrivial biaxial solutions  $q_i(z) \neq 0$  exist at sufficiently high local densities  $\rho_i(z) \geq \rho_i^{(UB)}(z)$  with the UB transition densities following from an expansion of the logarithms in Eq. (18):

$$\frac{3}{2[1 - s_1(z)]} = \rho_1^{(UB)}(z)L_1^2 D + \frac{[1 - s_2(z)]}{[1 - s_1(z)]} \rho_2^{(UB)}(z)L_2^2 D. \quad (19)$$

In the case of a monodisperse hard-rod fluid Eq. (19) reduces to Eq. (16). Since  $s_1(z) = s_2(z) = -1/2$  close to the wall, local biaxiality sets in if  $\rho_1(z) + L_2^2/L_1^2 \rho_2(z) = 1$  near the wall. We notice that, independent of the size ratios of the rods, biaxiality of one species of the fluid is

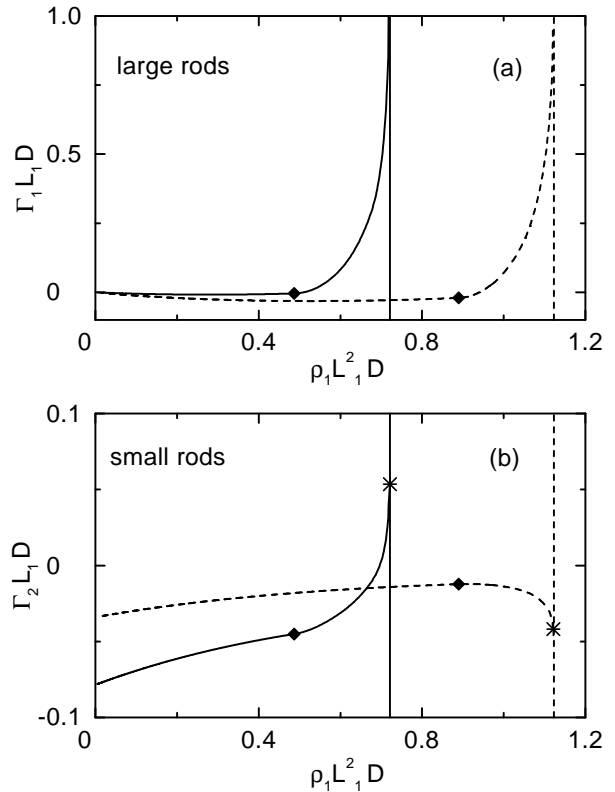


FIG. 5: The excess adsorptions  $\Gamma_1$  and  $\Gamma_2$  of large ((a)) and small ((b)) rods, respectively, ( $L_1 = 2L_2$ ,  $L_1/D \rightarrow \infty$ ) near a hard wall as a function of the bulk density  $\rho_1$  of the large rods for two values of the bulk density of the small rods:  $\rho_2 L_1^2 D = 2$  (solid lines),  $\rho_2 L_1^2 D = 0.5$  (dashed lines). The corresponding thermodynamic paths are indicated in Fig. 3 (a). The diamonds and the vertical lines mark the location of the uniaxial-biaxial transition densities  $\rho_1^{(UB)}$  and the densities of the isotropic bulk phase at isotropic-nematic coexistence  $\rho_1^{(I)}$ , respectively. For comparison,  $\rho_1^{(UB)}$  and  $\rho_2$  are marked by the dotted line and arrows in the bulk phase diagram displayed in Fig. 3 (a).  $\Gamma_1$  diverges logarithmically as  $\rho_1 \rightarrow \rho_1^{(I)}$ , while  $\Gamma_2$  attains finite values (\*) via square-root cusp singularities.

always accompanied by biaxiality of the other species, as expected on geometrical grounds.

## V. BINARY HARD-ROD AND HARD-PLATELET FLUIDS CONFINED BY TWO PARALLEL HARD WALLS

The results of the previous section show that a hard wall favors planar nematic order (the main body of the particles is oriented parallel to the wall) over isotropic order upon increasing the particle densities. We now consider binary hard-rod and hard-platelet fluids confined by two parallel hard walls at  $z = 0$  and  $z = H$  and investigate a possible capillary condensation of a nematic

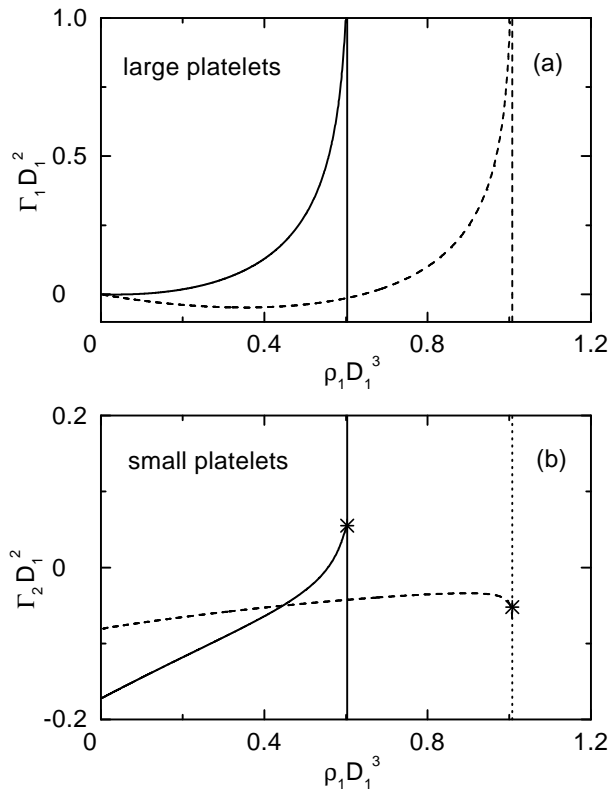


FIG. 6: The excess adsorptions  $\Gamma_1$  and  $\Gamma_2$  of large ((a)) and small ((b)) platelets, respectively, ( $D_1 = 2^{2/3}D_2$ ) near a hard wall as a function of the bulk density  $\rho_1$  of the large platelets for two values of the bulk density of the small platelets:  $\rho_2 D_1^3 = 2$  (solid lines),  $\rho_2 D_1^3 = 0.5$  (dashed lines). The corresponding thermodynamic paths are indicated in Fig. 3 (a). The vertical lines mark the locations of the densities of the isotropic phase at isotropic-nematic coexistence  $\rho_1^{(I)}$ .  $\Gamma_1$  diverges logarithmically as  $\rho_1 \rightarrow \rho_1^{(I)}$ , while  $\Gamma_2$  attains finite values (\*) via square-root cusp singularities.

phase. Particularly, we calculate the surface contributions defined via

$$\Omega[\rho_\alpha^{(i)}(z)] = V\omega_b + 2A\gamma_{wI} + A\omega(H), \quad (20)$$

where  $A$  is the area of a single surface,  $\omega_b$  is the bulk grand-canonical potential density, and  $V$  is defined as the volume of the container with its surface given by the position of the rim of the particles at closest approach so that  $V = AH$ .  $\gamma_{wI}$  is the wall – isotropic liquid surface tension in the absence of the second wall and  $\omega(H)$  is the finite size contribution. We restrict our attention to chemical potentials  $\mu_i$  smaller than the chemical potentials  $\mu_i^{(IN)}$  at bulk isotropic-nematic coexistence.

### A. Surface tensions and wetting at a single hard wall

Figure 7 displays the surface tension  $\gamma_{wI}$  as a function of the chemical potential of the larger particles. The steric interaction between the particles, which is more pronounced for the platelets, increases the surface tension with increasing chemical potential. On the other hand, nematic ordering of the particles, induced by the walls, leads to a decrease of the surface tension for large chemical potentials. For fixed small chemical potential  $\mu_2$  of the small particles a maximum of  $\gamma_{wI}$  as a function of the chemical potential  $\mu_1$  of the large particles is observed.

For large negative chemical potentials, i.e., in the limit of noninteracting particles, the wall – isotropic liquid surface tension is given by

$$\frac{\gamma_{wI}L_1D}{k_B T} = \frac{1}{2} \left[ \exp\left(\frac{\mu_1}{k_B T}\right) + \frac{L_2}{L_1} \exp\left(\frac{\mu_2}{k_B T}\right) \right] \quad (21)$$

for the binary rod fluid, and

$$\frac{\gamma_{wI}D_1^2}{k_B T} = \exp\left(\frac{\mu_1}{k_B T}\right) + \frac{D_2}{D_1} \exp\left(\frac{\mu_2}{k_B T}\right) \quad (22)$$

for the binary platelet fluid. The prefactor  $1/2$  in Eq. (21) reflects the fact, that the orientationally averaged excluded volume due to the wall is smaller for rods than for platelets.

For the binary rod mixture  $\gamma_{wI}$  is a non-monotonic function of  $\mu_1$  close the uniaxial-biaxial transition. The local minimum of  $\gamma_{wI}$  displayed in the inset of Fig. 7 disappears upon increasing or decreasing  $\mu_2$ , i.e., in the limit of monodisperse fluids.

We have confirmed that complete wetting of the wall – isotropic liquid interface by a nematic film occurs along the whole isotropic-nematic coexistence by observing a vanishing contact angle  $\vartheta$ :

$$\cos \vartheta = \frac{\gamma_{wI}(\mu_i^{(IN)}) - \gamma_{wN}(\mu_i^{(IN)})}{\gamma_{IN}}. \quad (23)$$

Here  $\gamma_{wI}(\mu_i^{(IN)})$  is the wall – isotropic liquid surface tension,  $\gamma_{wN}(\mu_i^{(IN)})$  is the wall-nematic liquid surface tension, and  $\gamma_{IN}$  is the isotropic-nematic interfacial tension. All tensions are taken at isotropic-nematic two-phase coexistence. The chemical potentials at the IN transitions are denoted by  $\mu_i^{(IN)}$  (see Fig. 3 (b)).

### B. Film geometry

The results for the finite size contribution  $\omega(H)$  are shown in Fig. 8. For sufficiently large slit widths  $H$  the slope of  $\omega(H)$  as a function of the chemical potential of the large particles changes discontinuously at a critical value, signalling a first-order capillary nematization

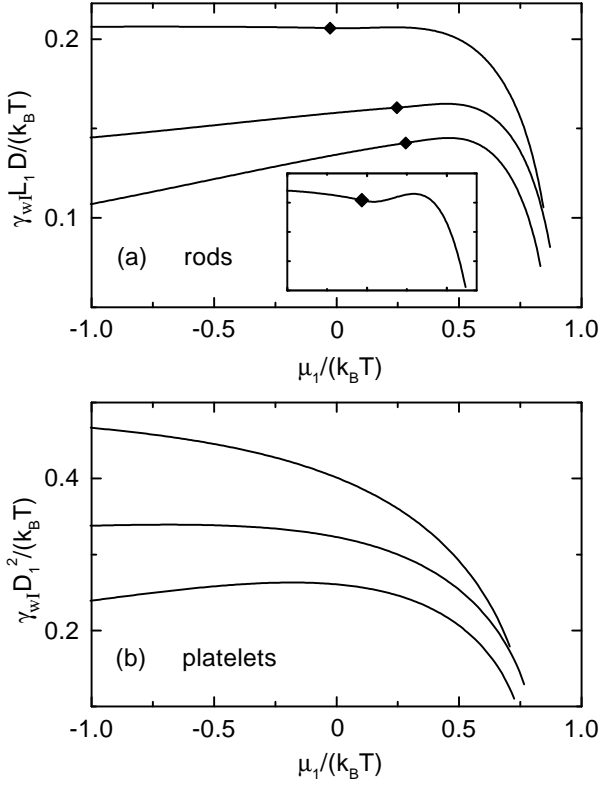


FIG. 7: The wall – isotropic liquid surface tension  $\gamma_{wI}$  of a binary hard-rod fluid ( $L_1 = 2L_2$ ,  $L_1/D \rightarrow \infty$ ), (a), and a binary hard-platelet fluid ( $D_1 = 2^{2/3}D_2$ ), (b), respectively. The chemical potential of the small particles is kept fixed for each curve and increases from bottom to top:  $\mu_2/(k_B T) = -1, 0, 1$ . Bulk isotropic-nematic coexistence occurs at  $\mu_1 = \mu_1^{(IN)}(\mu_2)$ , which corresponds to the final points of the curves at the right (see Fig. 3 (b)). The inset displays  $\gamma_{wI}$  of the binary hard-rod fluid for  $\mu_2/(k_B T) = 1$  with increased resolution. The diamonds mark the uniaxial-biaxial transitions.

transition. We emphasize that  $\omega(H)$  is a smooth and monotonic function of  $\mu_1$  for fixed  $H$  close to the uniaxial-biaxial transition whereas as discussed above  $\gamma_{wI}$  exhibits a local minimum for binary rod mixtures close to the uniaxial-biaxial transition. As function of  $H$  the finite size contribution  $\omega(H)$  corresponds to the solvation free energy for the immersed two plates acting as the confining walls for the fluid. According to the insets in Fig. 8,  $\omega(H)$  exhibits a minimum at  $H = 0$  (by construction,  $\omega(0) = -2\gamma_{wI}$  and  $\omega(\infty) = 0$ ) so that the solvation force  $-d\omega(H)/dH$  is attractive. For a discussion on the repercussions of this solvation force in the context of colloidal stability we refer to, e.g., Ref. [19]. Whereas for the present systems  $\gamma_{wI} > 0$  (see Fig. 7), for simple fluids the surface tension  $\gamma_{wl}$  is typically negative whenever the wall-liquid attractions dominate over liquid-liquid attractions and even for hard walls  $\gamma_{wl} < 0$  at densities well above liquid-vapor coexistence for which drying does not occur. In those situations  $\omega(0) > 0$  and the solvation

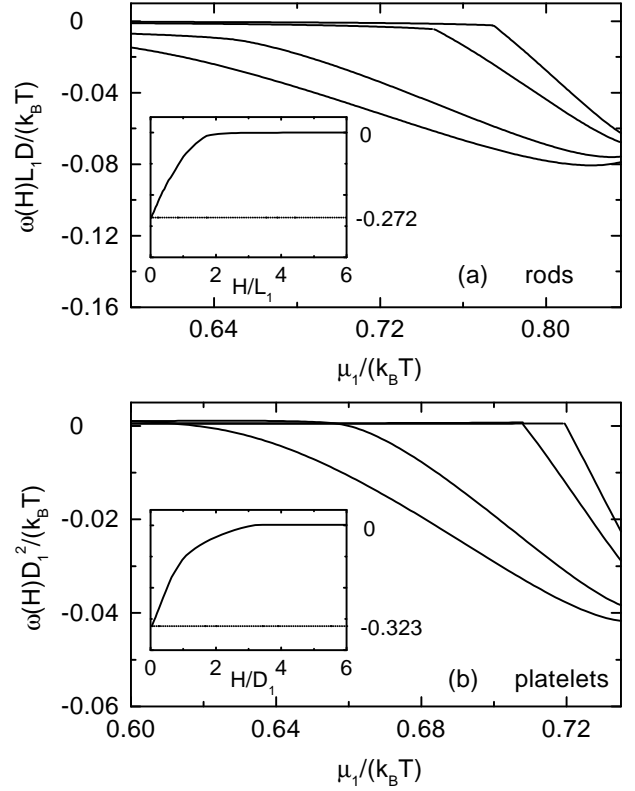


FIG. 8: The finite size contribution  $\omega(H)$  of the grand potential functional [see Eq. (20)] of a binary hard-rod fluid ( $L_1 = 2L_2$ ,  $L_1/D \rightarrow \infty$ ), (a), and a binary hard-platelet fluid ( $D_1 = 2^{2/3}D_2$ ), (b), respectively, confined in a slit of width  $H$ , and in contact with an isotropic bulk reservoir at chemical potential  $\mu_1$ . The chemical potential of the small particles is kept fixed at  $\mu_2/(k_B T) = -1$ . The width of the slit increases from top to bottom:  $H/L_1 = 1.5, 1.75, 2.5, 3$  in (a) and  $H/D_1 = 3, 3.5, 5, 6$  in (b). Bulk isotropic-nematic coexistence occurs at  $\mu_1 = \mu_1^{(IN)}(\mu_2)$ , which are the maximum  $\mu_1$ -values displayed (see Fig. 3 (b)). The insets display the solvation free energy  $\omega(H)$  as function of  $H$  at  $\mu_1/(k_B T) = 0.64$ .

potential decreases as  $H$  increases.

The occurrence of the capillary condensed nematic phase can be inferred more directly from the density and nematic order profiles displayed in Fig. 9. The density profile of the capillary condensed nematic phase is characterized by a nematic phase throughout the slit, whereas the density profile of the coexisting phase decays toward an isotropic phase in the middle of the slit. As expected from the presence of purely repulsive walls, the total local midplane density  $\rho_1(H/2) + \rho_2(H/2)$  of the capillary condensed nematic phase is slightly smaller than the coexisting nematic bulk density  $\rho_1^{(N)} + \rho_2^{(N)}$ . For the binary rod fluid both the capillary condensed nematic phase and the nematic film in the coexisting isotropic phase are biaxially symmetric. The location of the uniaxial-biaxial transition has practically not been altered by the confinement.

It is apparent from Fig. 9 that the interfacial profile in the isotropic phase is larger for the platelet fluid than for the rod fluid because of the relatively smaller intermolecular interactions between rods as compared with those between platelets. We observe coexistence between the isotropic and the capillary condensed nematic phase provided  $H \geq H_c(\mu_1, \mu_2)$ . For sufficiently narrow slits ( $H < H_c(\mu_1, \mu_2)$ ) a sharp capillary nematization transition no longer occurs and is replaced by a steep but continuous filling. Hence the capillary nematization transition ends in a capillary critical point at a critical wall separation  $H_c(\mu_1, \mu_2)$ .

We have determined the capillary nematization transition for various slit widths and the phase diagrams for binary rod and binary platelet mixtures constructed as function of the chemical potentials and the slit widths are shown in Figs. 10 (a) and 11 (a). Upon decreasing the slit width ( $H \geq H_c(\mu_1, \mu_2)$ ) the capillary nematization transition is shifted to smaller chemical potentials reminiscent of the shift of the capillary condensation transition in confined simple liquids. Upon increasing the chemical potential  $\mu_2$  of the small particles the critical wall separation decreases because the small particles are preferentially in the isotropic phase in the middle of the slit. This leads to a depletion of the large particles in the middle of the slit and prevents a continuous filling of the slit even for rather small slit widths.

Figures 10 (b) and 11 (b) display an alternative representation of the capillary phase diagrams in terms of average number densities defined as

$$\langle \rho_i \rangle = \frac{1}{H} \int_0^H dz \rho_i(z). \quad (24)$$

Here the curves with low values of  $\langle \rho_i \rangle$  represent the coexisting isotropic phase and the curves with high values of  $\langle \rho_i \rangle$  the capillary condensed nematic phase. Upon approaching the critical point ( $H < H_c(\langle \rho_1 \rangle, \langle \rho_2 \rangle)$ ) the difference of the average densities in the coexisting phases becomes smaller and vanishes at the critical point. The shape of the coexistence curves in Figs. 10 (b) and 11 (b) reflects the fact that the difference in  $\langle \rho_i \rangle$  between the two phases is used as order parameter. Our calculations lead to mean-field order parameter exponents; hence the dash-dotted lines in Figs. 10 (b) and 11 (b) do not intersect under an acute angle. The actual rounding becomes visible only at higher resolutions.

## VI. SUMMARY

We have applied a density-functional theory to fluids consisting of binary hard-platelets and hard-rods near a single hard wall or confined in a slit pore of width  $H$ . The particles are square parallelepipeds with orientations restricted to three mutually perpendicular directions (Fig. 1). The rectangular shape of the particles and

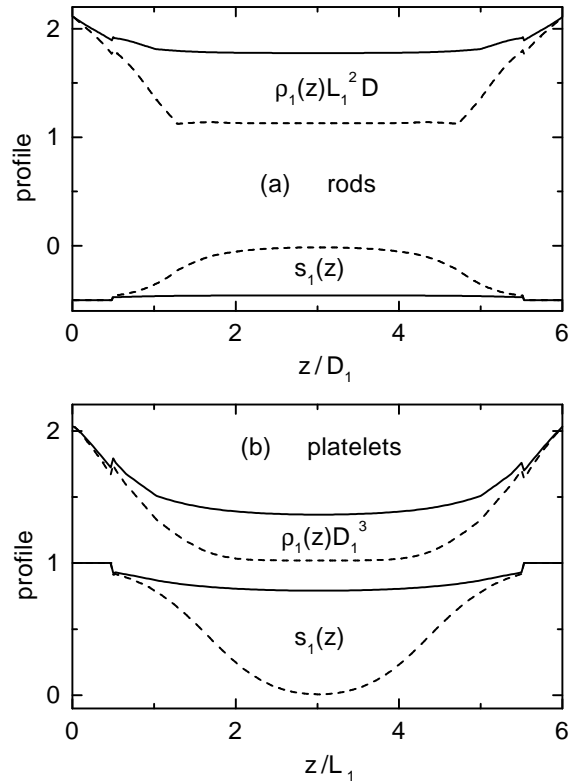


FIG. 9: Coexisting isotropic and capillary condensed nematic profiles for a binary hard-rod fluid ( $L_1 = 2L_2$ ,  $L_1/D \rightarrow \infty$ ), (a), and a binary hard-platelet fluid ( $D_1 = 2^{2/3}D_2$ ), (b), confined in a slit of width  $H = 6L_1$  and  $H = 6D_1$ , respectively. The isotropic profiles of the large particles (dashed lines) are characterized by  $s_1(z) = 0$  in the central region, while negative [positive] values of the nematic order parameters  $s_1(z)$  close to the confining walls at  $z = 0$  and  $z = 6L_1$  [ $z = 6D_1$ ] indicate that the rods [platelets] are aligned parallel to the walls. The capillary condensed nematic phase (solid lines) is characterized by strong orientational ordering ( $s_1(z) \neq 0$ ) throughout the slit. The chemical potential of the small particles is  $\mu_2/(k_B T) = -1.0$  so that in the bulk  $\rho_2^{(I)} L_1^2 D = 0.44$  and  $\rho_1^{(I)} L_1^2 D = 1.14$  in (a) and  $\rho_2^{(I)} D_1^3 = 0.44$  and  $\rho_1^{(I)} D_1^3 = 1.02$  in (b).

their restricted orientations allow one, within the framework of a third-order virial approximation of the excess free energy functional, to determine numerically the density profiles, orientational profiles, surface and finite-size contributions to the grand potential, and phase diagrams with the following main results.

(1) Figures 2 and 3 demonstrate that the bulk isotropic-nematic transition of the binary platelet mixture (size ratio:  $D_1 = 2^{2/3}D_2$ , where  $D_i \times D_i$  is the surface size of the thin platelets of species  $i$ ) occurs at a smaller density than for the rod mixture (size ratio:  $L_1 = 2L_2$ , where  $L_i$  is the length of the thin rods of species  $i$ ). Moreover, the density gap at the isotropic-nematic transition is smaller for the rod fluid than for

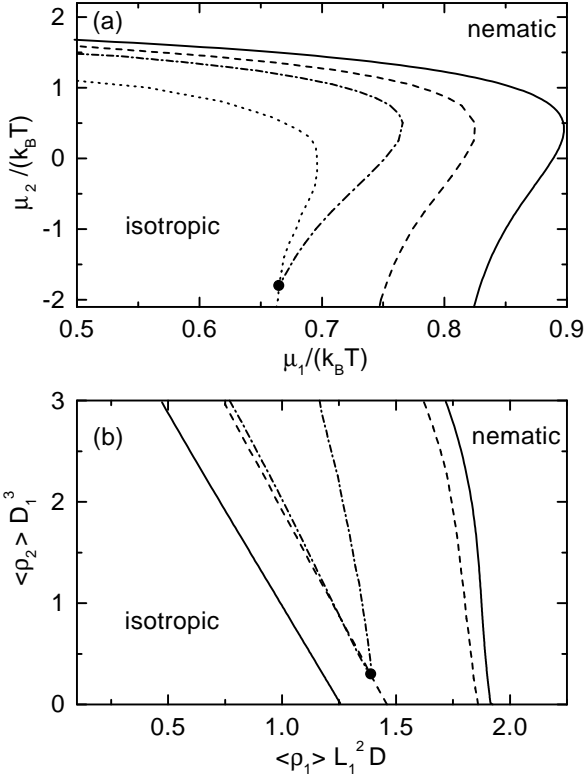


FIG. 10: (a) Phase diagram of a confined binary hard-rod fluid ( $L_1 = 2L_2$ ,  $L_1/D \rightarrow \infty$ ) as a function of the chemical potentials  $\mu_1$ ,  $\mu_2$ , and wall separation  $H$ . The solid line represents the bulk phase diagram (see Fig. 3 (a)), while the dashed and the dash-dotted lines correspond to wall separations  $H = 6L_1$  and  $H = 2L_1$ . For fixed  $H < H_c(\mu_1, \mu_2)$  the capillary condensation transition is first order and terminates at a critical point. These critical points for various slit widths form the dotted line. One example of such a capillary critical point is indicated by the solid circle. There the corresponding line of first-order capillary transitions for  $H = 2L_1$  (dash-dotted line) ends. (b) Phase diagram of the same fluid plotted (with the same line code as in (a)) as function of the average number densities  $\langle \rho_1 \rangle$  and  $\langle \rho_2 \rangle$  in the slit. In between corresponding lines there is two-phase coexistence between isotropic and capillary condensed nematic phases. For a small slit width  $H = 2L_1$  (dash-dotted line) the branches of the coexisting capillary condensed nematic phase and isotropic phase end at a critical point denoted by the solid circle.

the platelet fluid because of larger intermolecular interactions between platelets as compared with those of rods.

(2) Platelets [rods] lying very closely to a planar hard wall must adopt a fully parallel alignment (see Fig. 1), so that the nematic order parameters (Eq. (11)) reach their limiting values  $s_i(0) = 1$  [ $s_i(0) = -1/2$ ] there (Fig. 4). The biaxial order profiles (Eq. (12)) for the inhomogeneous fluids at densities slightly below the bulk isotropic-nematic transition densities demonstrate biaxial symmetry ( $q_i(0) \neq 0$ ) of rods and uniaxial symmetry ( $q_i(0) = 0$ ) of platelets near the wall (Fig. 4).

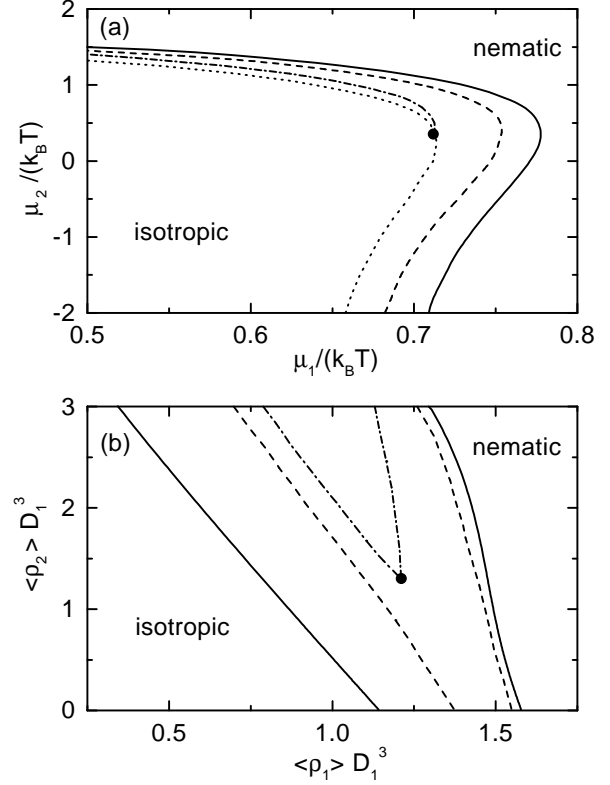


FIG. 11: Phase diagrams of a confined binary hard-platelet fluid ( $D_1 = 2^{2/3}D_2$ ). The solid lines represent the bulk phase diagram (see Fig. 3), while the dashed and the dash-dotted lines correspond to wall separations  $H = 6D_1$  and  $H = 2D_1$ . The critical points for various slit widths form the dotted line in (a).

(3) The excess adsorption  $\Gamma_1$  of the large particles diverges logarithmically as  $\rho_1 \rightarrow \rho_1^{(I)}$ , where  $\rho_1^{(I)}$  is the bulk density of the large particles in the isotropic phase at the isotropic-nematic transition (Figs. 5 and 6). Complete wetting of the wall – isotropic liquid interface by a nematic film is confirmed by observing a vanishing contact angle.

(4) The steric interaction between the particles increases the wall – isotropic liquid surface tension  $\gamma_{wI}$  with increasing chemical potential, whereas nematic ordering of the particles, induced by the walls, leads to a decrease of the surface tension for large chemical potentials (Fig. 7).

(5) For sufficiently large slit widths the slope of the finite size contribution to the grand potential as a function of the chemical potential of the large particles changes discontinuously at a critical value, signaling a first-order capillary nematization transition (Fig. 8). The density profile of the capillary condensed nematic phase is characterized by a nematic phase throughout the slit, whereas the density profile of the coexisting phase decays toward an isotropic phase in the middle of the slit (Fig. 9). The isotropic-nematic interfacial profile is broader for the

platelet fluid than for the rod fluid.

(6) Coexistence between the isotropic and the capillary condensed nematic phase is observed provided the slit width  $H$  is sufficiently large:  $H \geq H_c(\mu_1, \mu_2)$ . For suf-

ficiently narrow slits ( $H < H_c(\mu_1, \mu_2)$ ) a sharp capillary nematization transition no longer occurs and is replaced by a steep but continuous filling (Figs. 10 and 11).

- 
- [1] See e.g., G. C. Maitland, *Current Opinion in Colloid and Interface Science* **5**, 301 (2000).
- [2] A. B. D. Brown, S. M. Clarke, and A. R. Rennie, *Langmuir*, **14**, 3129 (1998).
- [3] F. M. van der Kooij and H. N. W. Lekkerkerker, *J. Phys. Chem. B* **102**, 7829 (1998).
- [4] A. B. D. Brown, C. Ferrero, T. Narayanan, and A. R. Rennie, *Eur. Phys. J. B* **11**, 481 (1999).
- [5] F. M. van der Kooij and H. N. W. Lekkerkerker, *Phil. Trans. R. Soc. Lond. A* **359**, 985, (2001).
- [6] F. M. van der Kooij, D. van der Beek, and H. N. W. Lekkerkerker, *J. Phys. Chem. B*, **105**, 1696, (2001).
- [7] M. A. Bates and D. Frenkel, *J. Chem. Phys.* **110**, 6553, (1999).
- [8] A. Galindo, G. Jackson, and D. J. Photinos, *Chem. Phys. Lett.*, **325**, 631, (2000).
- [9] L. Harnau, D. Costa, and J.-P. Hansen, *Europhys. Lett.* **53**, 729 (2001).
- [10] H. H. Wensink, G. J. Voerge, and H. N. W. Lekkerkerker, *J. Phys. Chem. B*, **105**, 10610, (2001).
- [11] H. H. Wensink, G. J. Voerge, *Phys. Rev. E*, **65**, 031716, (2002).
- [12] L. Harnau and S. Dietrich, *Phys. Rev. E*, **65**, 021505 (2002).
- [13] R. Zwanzig, *J. Chem. Phys.* **39**, 1714 (1963).
- [14] L. Onsager, *Ann. (N.Y.) Acad. Sci.* **51**, 627 (1949).
- [15] R. van Roij, M. Dijkstra, and R. Evans, *Europhys. Lett.* **49**, 350 (2000).
- [16] R. van Roij, M. Dijkstra, and R. Evans, *J. Chem. Phys.* **113**, 7689 (2000).
- [17] M. Dijkstra, R. van Roij, and R. Evans, *Phys. Rev. E* **63**, 051703 (2001).
- [18] N. Clarke and T. C. B. McLeish, *J. Phys. II France*, **2**, 1841 (1992).
- [19] Y. Mao, M. E. Cates and H. N. W. Lekkerkerker, *Phys. Rev. Lett.* **75**, 4548 (1995).